Atmos. Meas. Tech., 11, 1689–1705, 2018
https://doi.org/10.5194/amt-11-1689-2018
© Author(s) 2018. This work is distributed under
the Creative Commons Attribution 3.0 License.

Atmospheric Measurement Techniques
Open Access
EGU

Atmospheric characterization through fused mobile airborne and surface in situ surveys: methane emissions quantification from a producing oil field

Ira Leifer[1], Christopher Melton[1], Marc L. Fischer[2], Matthew Fladeland[3], Jason Frash[1], Warren Gore[3], Laura T. Iraci[3], Josette E. Marrero[3], Ju-Mee Ryoo[3], Tomoaki Tanaka[3], and Emma L. Yates[3]

[1]Bubbleology Research International, Solvang, CA 93463, USA
[2]Lawrence Berkeley National Laboratory, 1 Cyclotron Road, Berkeley, CA 94720, USA
[3]NASA Ames Research Center, Moffett Field, CA 94035, USA

Correspondence: Ira Leifer (ira.leifer@bubbleology.com)

Received: 27 April 2017 – Discussion started: 1 June 2017
Revised: 15 December 2017 – Accepted: 9 January 2018 – Published: 27 March 2018

Abstract. Methane (CH_4) inventory uncertainties are large, requiring robust emission derivation approaches. We report on a fused airborne–surface data collection approach to derive emissions from an active oil field near Bakersfield, central California. The approach characterizes the atmosphere from the surface to above the planetary boundary layer (PBL) and combines downwind trace gas concentration anomaly (plume) above background with normal winds to derive flux. This approach does not require a well-mixed PBL; allows explicit, data-based, uncertainty evaluation; and was applied to complex topography and wind flows.

In situ airborne (collected by AJAX – the Alpha Jet Atmospheric eXperiment) and mobile surface (collected by AMOG – the AutoMObile trace Gas – Surveyor) data were collected on 19 August 2015 to assess source strength. Data included an AMOG and AJAX intercomparison transect profiling from the San Joaquin Valley (SJV) floor into the Sierra Nevada (0.1–2.2 km altitude), validating a novel surface approach for atmospheric profiling by leveraging topography. The profile intercomparison found good agreement in multiple parameters for the overlapping altitude range from 500 to 1500 m for the upper 5 % of surface winds, which accounts for wind-impeding structures, i.e., terrain, trees, buildings, etc. Annualized emissions from the active oil fields were 31.3 ± 16 Gg methane and 2.4 ± 1.2 Tg carbon dioxide. Data showed the PBL was not well mixed at distances of 10–20 km downwind, highlighting the importance of the experimental design.

1 Introduction

1.1 Methane trends and uncertainty

On decadal timescales, methane (CH_4) affects the atmospheric radiative balance more strongly than carbon dioxide (CO_2) (IPCC, 2007, Fig. 2.21). Since pre-industrial times, CH_4 emissions have risen by a factor of 2.5 (Dlugokencky et al., 2011; Khalil and Rasmussen, 1995), while estimates of its lifetime has decreased; it is now estimated at ~ 8.5 years (Sonnemann and Grygalashvyly, 2014). Atmospheric CH_4 growth almost ceased between 1999 and 2006 but has resumed since 2007 (Nisbet et al., 2014; Schwietzke et al., 2016). Several processes are proposed to underlie this trend (Ghosh et al., 2015; John et al., 2012), with recent isotopic shifts suggesting wetlands are the dominant driver (Nisbet et al., 2016); however, high uncertainty in emission inventories (IPCC, 2013) complicates interpretation of the underlying mechanism(s).

The dominant CH_4 loss arises from reaction with hydroxyl (OH), whose concentration has been increasing in recent decades (John et al., 2012), causing a decrease in the estimated CH_4 lifetime of $0.5\,\%\,yr^{-1}$ (Karlsdóttir and Isaksen, 2000). Overall, the estimate of the CH_4 lifetime has decreased by $\sim 40\,\%$ from an estimated 12 years in 2007 (IPCC, 2007). Rigby et al. (2017) suggest a decline in OH is likely to have contributed to increasing CH_4 since 2007. The recent discovery of a new significant CH_4 loss mechanism,

terrestrial uptake (Fernandez-Cortes et al., 2015), illustrates the need to understand loss mechanisms better (Allen, 2016).

Large CH_4 budget uncertainties remain for many sources (IPCC, 2013) with greater uncertainty in future trends from global warming feedback (Rigby et al., 2008) and increasing anthropogenic activities (Kirschke et al., 2013; Saunois et al., 2016; Wunch et al., 2009). Emphasizing these uncertainties are recent studies that suggest underestimation by a factor of 1.5 in the important anthropogenic CH_4 source, fossil fuel industrial (FFI) emissions (Brandt et al., 2014). Tellingly, this discrepancy was only noted recently (Miller et al., 2013), in part because the US CH_4 monitoring network is too sparse to constrain emissions at "regional to national scales" (Dlugokencky et al., 2013). Furthermore, isotopic data indicate even larger underestimation by a factor of 1.6–2.1 (Schwietzke et al., 2016). FFI emissions are the largest (Brandt et al., 2014; EPA, 2017) or second-largest, after agriculture (Saunois et al., 2016), anthropogenic contributor to the global CH_4 budget. These uncertainties strongly argue for the need for new, robust methodologies for flux derivation.

1.2 Methane flux estimation

Various approaches have been developed to derive surface emissions from CH_4 concentration measurements including direct flux assessment – i.e., measurement of winds and concentrations through a plane – and/or by the comparison of upwind and downwind mass budgets (Peischl et al., 2015, 2016; White et al., 1976), data-driven mass balance (e.g., Karion et al., 2013), tracer / tracer ratio (LaFranchi et al., 2013), and assimilation inverse models (e.g., Jeong et al., 2013, 2012; Saunois et al., 2017). Challenges for the last of those approaches include the needs for accurate meteorological transport models and good a priori emission distributions (Miller et al., 2013; Peischl et al., 2016; Smith et al., 2015). Miller et al. (2013) concluded that bottom-up inventories (EPA, 2013; European Commission, 2010) significantly underestimate husbandry and FFI emissions. To apportion CH_4 to FFI versus biological sources, the tracer–tracer approach has been applied using ethane, whose emission ratio to CH_4 requires tight constraint (Peischl et al., 2013; Simpson et al., 2012; Wennberg et al., 2012). In practice, this emission ratio is an a priori assumption in the assessment.

Direct assessment approaches have advantages over inversion approaches. Direct approaches allow explicit uncertainty evaluation and do not require an a priori emission spatial distribution, which may be unknown. Direct approaches also do not require the ability to model atmospheric transport accurately across the study region. In areas of complex topography or highly variable winds, this transport can challenge assimilation approaches, which also are challenged in areas with poorly characterized (or unknown) or highly variable sources, particularly if the measurement network is sparse. For direct assessment approaches, data collection should be rapid if winds and/or emissions are variable and at adequate data density to characterize fine-scale structure.

1.3 Study motivation

Herein we report on a novel application of fused airborne and surface in situ data to directly estimate CH_4 emissions using an anomaly approach rather than a more typical mass balance approach due to a lateral gradient in the upwind data. A direct approach does not require accurate winds over the study domain, only in the measurement plane. The approach was applied to 1164 km of airborne data collected on 19 August 2015 by NASA's Alpha Jet Atmospheric eXperiment (AJAX), while AMOG (AutoMObile greenhouse Gas) Surveyor collected 1074 km of contemporaneous mobile surface data. Both platforms measure carbon dioxide (CO_2), CH_4, water vapor (H_2O), and ozone (O_3), as well as winds, pressure, relative humidity (RH), and temperature (T). The surface and airborne datasets were collected in a downwind curtain or plane oriented approximately orthogonal to the winds, to characterize the full planetary boundary layer (PBL) from surface to above the PBL.

Additionally, the surface survey route was designed to include an ascent to ~ 2.2 km above sea level to allow PBL characterization. Data fusion between measurement platforms was validated by a vertical profile intercomparison for 0.5 to 1.5 km altitude by AMOG Surveyor leveraging topographic relief.

1.4 The southern San Joaquin Valley, California

Most California oil production lies in the San Joaquin Valley (SJV), as do most of California agriculture, including many intensive dairies (Gentner et al., 2014), and major north–south transportation arteries. For this study, data were collected for the Kern River oil fields (Kern Front oil field, Kern River oil field, and the Poso Creek oil field, referred to herein as the Kern Fields), located adjacent to northwest Bakersfield (Fig. 1a). These adjacent oil fields create a strong CH_4 source that largely is isolated from confounding plumes from other SJV sources. This area includes complex wind flow patterns across and around the "toe" of Sierra Nevada foothills, which extend into the Kern Front and Kern River oil fields. Here, topographic steering ensures predictable prevailing northwesterly winds blow across the Kern Fields.

Strong orographic forcing also arises from tall bluffs (~ 100 m) on the Kern River Valley's south bank, which separates the Kern River oil field from the urban city of Bakersfield (pop. 364 000 in 2013). The fine-scale wind structure that results from orographic forcing on transport dictated an anomaly approach for flux derivation, as did the presence of strong CH_4 structures (plumes) in the valley's lowest air. In the anomaly approach, transects must extend beyond a reasonably well defined plume.

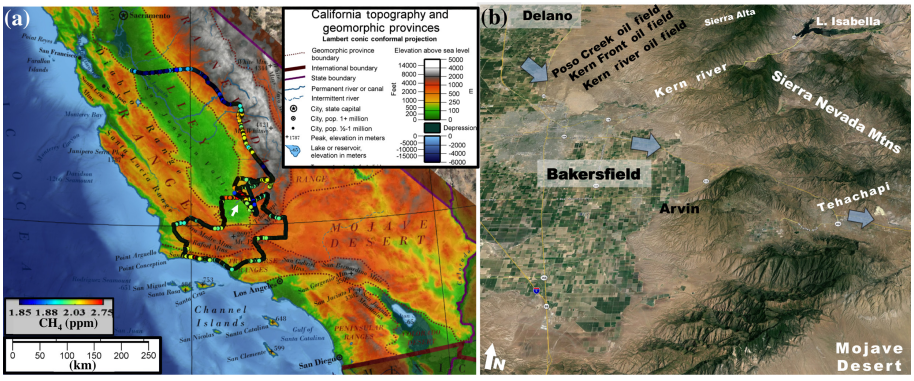

Figure 1. (a) Full surface and airborne data for 19 August 2015 mapped over California topography. White arrow shows Bakersfield. Data key in panel. **(b)** Study area map showing direction of daytime prevailing winds and nearby mountain topography (Google Earth, 2016). See Supplement Fig. S1 for a high-altitude (20 km) photo of the entire study area and surrounding terrain.

Topography (i.e., mountain ranges) plays a locally dominant role in overall southern California airflows, where upper-level winds locally force the lower-level flows that transport pollutants (Bao et al., 2008). The SJV is delimited on the east by the Sierra Nevada and on the west by the coastal Transverse Ranges (Fig. 1a). Transport between the SJV and adjacent air basins is poor due to California's mountain ranges. The SJV features weak surface winds (Bao et al., 2008), with the worst air quality in the United States occurring in the cities of Bakersfield and Delano (American Lung Association, 2016) in the SJV.

Pacific Ocean air primarily enters the SJV through the San Francisco Bay area and the Carquinez Strait, where it splits north into the Sacramento Valley and south into the SJV (Zhong et al., 2004). This flow extends up to ∼ 1 km altitude (Zhong et al., 2004). These winds are near orthogonal to the 600 km long Central Valley of California – i.e., cross-slope. South of Bakersfield, winds shift to from the west due to mountains that guide SJV air out into the Mojave Desert, where it affects air quality for up to hundreds of kilometers distant (VanCuren, 2015). Although the Tehachapi Pass is the main exit pathway of SJV air, other passes also transport air into the Mojave Desert. These flows are augmented by high inland temperatures relative to the Pacific Ocean, which creates a horizontal pressure gradient that drives local upslope flows during the day and returning downslope nocturnal flows (Zhong et al., 2004). The pressure gradient is maximal around sunset, although winds peak ∼ 4 h later, shortly before midnight. This pressure gradient is controlled by the semi-permanent Pacific high, situated offshore central California, which diverts storms far to the north during summer. This pressure feature drives prevailing west-southwesterly winds at the regional scale in the California south coast air basins (Boucouvala and Bornstein, 2003).

2 Methodology

2.1 Experimental design

Data were collected as part of the GOSAT-COMEX Experiment (Greenhouse gases Observing SATellite–CO_2 and Methane Experiment (GCE)) campaign. GCE was developed to characterize emissions on spatial scales from decameter (in situ surface, imaging spectroscopy) to kilometer (in situ airborne) to deca-kilometer (satellite) in an area of complex topography. GCE design combined in situ mobile surface and airborne data with GOSAT satellite data. In situ data serve to assess the satellite pixel–plume overlap. Key GCE requirements are relatively steady, strong, isolated emissions and predictable, steady winds. Prevailing study area winds are from the west-northwest, veering to westerly winds to the southeast of Bakersfield (Fig. 1). Prevailing wind directions are highly reliable due to topographic control.

GCE developed from the COMEX campaign (Krautwurst et al., 2016), which combined in situ airborne and surface observations with both imaging and non-imaging spectroscopy to explore synergies for GHG emission estimation (Thompson et al., 2015). COMEX focused on southern California CH_4 sources, including husbandry, landfills, natural geology, and petroleum hydrocarbon refining and production.

GCE combines airborne and surface data collected at dramatically different speeds. AJAX collects data at $\sim 500\,\mathrm{km\,h^{-1}}$, capturing a snapshot of atmospheric winds and plume structure. Surface GCE data are collected quasi-Lagrangian, starting northwest (upwind) and proceeding southeast and then east (downwind). This enables useful data collection even when a CH_4 plume drifts into the study area after the upwind survey – data collection proceeds downwind faster than advection. The surface route was designed carefully to traverse all targeted GOSAT pixels using rarely used (low-traffic) surface roads and requires ∼ 100 min.

Airborne and surface surveys are timed so that the downwind data plane (Krings et al., 2011) is surveyed concurrent

with the satellite overpass. Data planes extend from the surface (AMOG) to above the PBL (AJAX), reducing uncertainty by providing a more complete atmospheric characterization including below where airplanes are permitted to fly ($\sim$ 500 m in an urban area). AJAX and AMOG profile data are fused by an interpolation approach that imposes the observed vertical structure, and the flux through the data curtain is calculated (Sect. 2.5).

GCE first incorporates an AMOG Surveyor upwind transit from Delano (100 m) on the SJV floor to Sierra Alta (1800 m) and higher to confirm that upwind CH_4 plumes do not threaten to impact the study area during the experiment; otherwise the survey is aborted. A key mission abort criterion is wind compliance. Specifically, winds must not be too light (typically less than $\sim 2\,m\,s^{-1}$) or variable ($>30°$) and must flush nocturnal accumulations before the GOSAT overpass (i.e., no CH_4 cloud at or nearby upwind of the site. This means that winds cannot be light as recently as several hours prior and must be prevailing. The upwind transit provides vertical profile information including PBL height and vertical structure. AJAX repeats this upwind transect to compare wind profiles with AMOG; however, discrepancies in the transects arise from the road following terrain and the airplane needing to avoid peaks along the ridge.

2.2 AMOG Surveyor

Mobile atmospheric surface measurements have been conducted for many years using a customized van (Lamb et al., 1995) or a recreational vehicle (Farrell et al., 2013; Leifer et al., 2013). Recently, the development of cavity-enhanced absorption spectroscopy (CEAS) analyzers has opened the way for rapid and highly accurate trace gas measurements (Leen et al., 2013) without the need for onboard compressed gases as in gas chromatography (Farrell et al., 2013), although periodic calibration with gas standards is important, albeit typically not on board the platform. This allows for smaller vehicle survey platforms at lower logistical overhead (Leifer et al., 2014; McKain et al., 2015; Pétron et al., 2012; Yacovitch et al., 2015). A competing sensor technology that has been used in mobile survey data collection is open-path spectroscopy (Sun et al., 2014). Mobile survey platforms can incorporate older technology such as fluorescence to, for example, measure ozone, O_3.

Mobile surface data were collected by AMOG Surveyor (Leifer et al., 2014), a modified commuter car (see Supplement Sect. S2.1 for additional details). AMOG Surveyor provides mobile high-speed, high-spatial-resolution observations of meteorology (winds, temperature, pressure), trace gases (greenhouse and others), and remote sensing parameters. AMOG Surveyor uses a range of trace gas analyzers and careful design with respect to wind flow around the vehicle to characterize strong spatial heterogeneity at up to highway speeds.

Two-dimensional winds are measured by a sonic anemometer (VMT700, Vaisala) mounted 1.4 m above the roof (at 3.0 m above the surface) and above vehicle flow streamlines for slow to highway speeds. Estimated accuracy is approximately 10° and $0.3\,m\,s^{-1}$ for wind speeds above $1.5\,m\,s^{-1}$ (see Supplement for further details).

A high-flow vacuum pump (GVB30, Edwards Vacuum) draws air down sample lines from 5 and 3 m above ground for GHG and ozone (O_3) analyzers. The 5 m sample line height references low speed/stopped (< a few $m\,s^{-1}$) AMOG sample collection. At high speed ($>10\,m\,s^{-1}$) the sample tube flexes backwards to 3 m height to avoid destructively hitting obstacles at high speed. This protects the sample line from hitting bridges, tree branches, etc. Greenhouse gases, CO_2, CH_4, and H_2O are measured at up to 10 Hz by an off-axis integrated cavity output spectrometer–cavity-enhanced absorption spectroscopy analyzer, with a 1 s accuracy of 1 ppb for CH_4 (ICOS-CEAS, 911-0010, Los Gatos Research, Inc.). Calibration is with a Scott-Marrin CH_4 and CO_2 atmospheric standard. A fluorescence analyzer measured O_3 at 0.25 Hz (49C, Thermo Fisher Scientific, MA, USA). This difference does not arise from calibration differences; the AMOG Surveyor O_3 analyzer was cross-calibrated with the AJAX calibration source to 1 ppb accuracy. AMOG Surveyor's full trace gas suite (carbonyl sulfide, carbon monoxide, nitric oxide, nitrogen dioxide, hydrogen sulfide, sulfur dioxide, total sulfur, ammonia) was not deployed on 19 August 2015.

The greenhouse gas analyzer is calibrated using a Scotty's whole-air standard before and/or after each data collection, with the calibration factor closest to the day of flight being applied to each raw CO_2 and CH_4 measurement. Calibration factors have been shown to agree within less than 1 ppb. The calibration factor includes a linear correction for cell pressure, which can drop at higher altitudes. This pressure calibration has been shown to be linear from 140 mtorr down to 28 mtorr.

Relevant recent AMOG Surveyor improvements since Leifer et al. (2014) include a high-speed thermocouple (50416-T, Cooper-Atkins) and a high-accuracy (0.2 hPa) pressure sensor (61320V RM Young Co.). Both are mounted in a passive roof radiation shield (7710, Davis Instruments) to largely eliminate dynamic pressure effects from the airflow. Position information is critical to accurate wind measurements and is provided by redundant (two) global navigation satellite systems (19X HVS, Garmin) that use the GLONASS, GPS, Galileo, and QZSS satellites at 10 Hz (WGS84). AMOG Surveyors' analyzers' and sensor data are logged asynchronously on a single computer. Custom software integrates the data streams and provides real-time visualization of multiple parameters in the Google Earth environment.

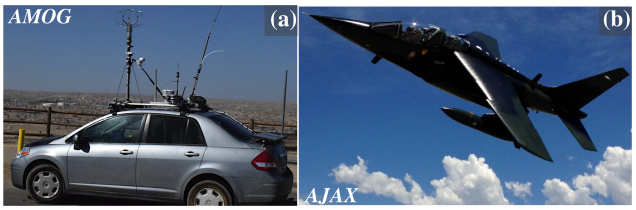

Figure 2. Study platforms. **(a)** AutoMObile trace Gas (AMOG) Surveyor, Kern River oil field in background. Photo courtesy of Ira Leifer. **(b)** The Alpha Jet Atmospheric eXperiment (AJAX) aircraft, photo courtesy of Akihiko Kuze, JAXA. See Supplement Sect. S1 for further details.

2.3 AJAX

AJAX (Fig. 2b) collected airborne in situ measurements of CO_2, CH_4, and H_2O by cavity ring-down spectroscopy (G2301-m, Picarro Inc.); O_3 (Model 205, 2B Technologies Inc.); and meteorological parameters including 3-D winds by the Meteorological Measurement System (https://earthscience.arc.nasa.gov/mms), a NASA-developed system with accuracy of $\pm 1\,\mathrm{m\,s^{-1}}$. The greenhouse gas analyzer is calibrated using NOAA whole-air standards; calibrations are performed before and/or after each flight, with the calibration factor closest to the day of flight being applied to each raw CO_2 and CH_4 measurement. Further corrections include applying water vapor corrections provided by Chen et al. (2010) to calculate CO_2 and CH_4 dry mixing ratios. Data are quality-control-filtered for deviations in instrument cavity pressure, to improve in-flight precision.

Overall CH_4 measurement uncertainty is typically <2.2 ppb, including contributions from accuracy of the standard, precision (1σ over 6 min), calibration repeatability, in-flight variance due to cavity pressure fluctuations, and uncertainty due to water corrections and pressure dependence (based on environmental chamber studies). See Hamill et al. (2016), Tanaka et al. (2016), and Yates et al. (2013) for further aircraft and instrumentation details, and Supplement Sect. S2.2.

2.4 Background estimation and data fusion

The flux ($Q(x, z)$) in moles per second per square meter with respect to lateral transect distance (x) and altitude (z) through the x–z plane is the product of the normal winds ($U_N(x, z)$) in meters per second and the plume concentration anomaly ($C'(x, z)$) or mole fraction in ppm (Leifer et al., 2016).

$$Q(x,z) = k(z)U_N(x,z)C'(x,z) = k(z)U_N(x,z)(C(x,z) - C_B(x,z)) \quad (1)$$

$k(z)$ converts from ppm to moles. Interpolation of C' and U_N is linear within the PBL and is assumed uniform above the PBL. To calculate $Q(x, z)$ requires C' relative to background ($C_B(x, z)$). Initially surface data that were collected for an upwind surface transect were used to derive C_B, using the assumption of vertical uniformity for "background".

Unfortunately, the upwind data showed a lateral gradient, which coupled with uncertainty in precisely where the downwind air originated (given the topography, which features a gentle incline towards the northeast, this gradient is unsurprising, in retrospect). Thus a very small shift in the winds between the upwind and downwind curtains results in a significant shift in C_B, with a very large effect on Q. As a result, the more traditional upwind–downwind mass balance approach was abandoned for an anomaly approach.

In the anomaly approach, $C_B(x, z)$ was derived from evaluating $C_B(x<x_{max}/2, z)$ and $C_B(x>x_{max}/2, z)$, denoted $C_{BL}(z)$ and $C_{BR}(z)$, respectively, where x_{max} is the lateral extent of the data curtain. Then, $C_B(x,z)$ was derived from a first-order linear polynomial fit of $C_{BL}(z)$ and $C_{BR}(z)$.

Both $C_{BL}(z)$ and $C_{BR}(z)$ are derived from the amplitude of a Gaussian fit to the left and right probability density functions ($\Phi_L(C(x<x_{max}/2, z))$ and ($\Phi_R(C(x>x_{max}/2, z))$, respectively, for each flight transect level. Specifically, for Φ_L and Φ_R, Gaussian functions are fit to model the plume distribution (Φ_P) and the background distribution (Φ_B). In these data, Φ_B is well fit by a single Gaussian, while Φ_P is best described by multiple Gaussian functions. Then, $C_{BL}(z)$ and $C_{BR}(z)$ are defined such that

$$\int \Phi_{BL}(C_{BL}(z)) = 0 \text{ and } \int \Phi_{BR}(C_{BR}(z)) = 0, \quad (2)$$

where Φ_{BL} and Φ_{BR} are the background Φ_B for the left and right halves of the data plane, respectively. Concentration is not a conserved value; thus C' is converted into mass (N') by the ideal gas law (k in Eq. 1) for spatial integration to derive the total emissions (E), which is the integration of the flux through the plane (Q):

$$E = \int_{x1}^{x2} \int_{0}^{z=\mathrm{PBL}} Q(x,z)\,\mathrm{d}z\mathrm{d}x. \quad (3)$$

Interpolation, prior to integration, is linear.

2.5 Uncertainty evaluation for emission calculation

The flux calculation has two source of uncertainty: accuracy and representativeness. Specifically, background concentration profiles may be incorrect, while winds, which are measured accurately, could be unrepresentative, as could concentrations due to temporal variability over the period needed to make the measurements. Monte Carlo simulations based on observed data variability were run to assess uncertainty. Instrumental accuracy uncertainty is far less than spatial and temporal variability. Thus, spatial and temporal variability are the dominant source of uncertainty (Leifer et al., 2016).

Monte Carlo simulations were based on 1 standard deviation in the observed $U_N(z)$ around the mean for each flight

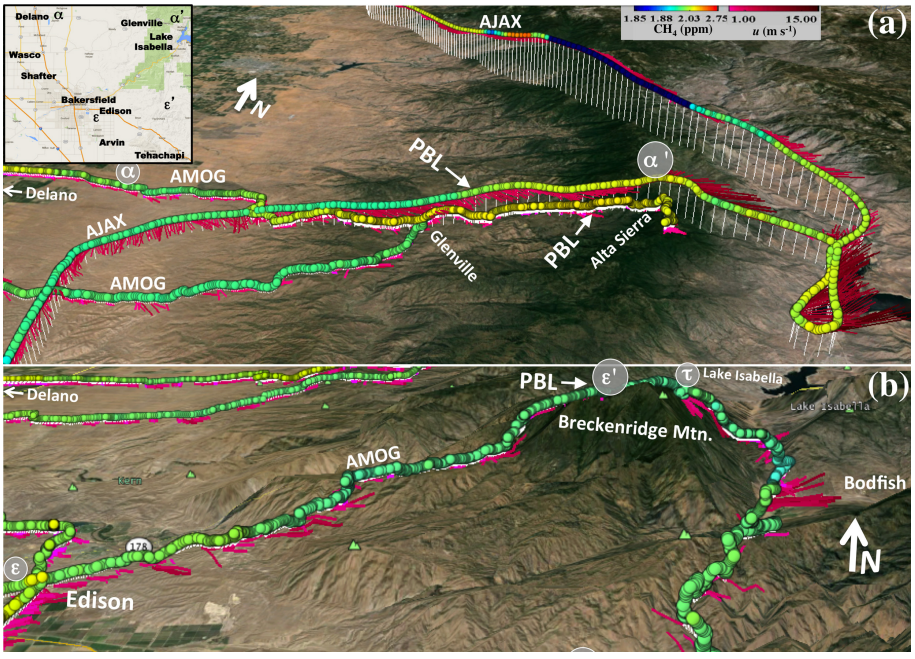

Figure 3. (a) Pre-survey, upwind AMOG surface and AJAX airborne methane (CH_4) and winds for vertical profile on the Delano–Alta Sierra transect ($\alpha - \alpha'$). Inset shows area map. **(b)** Post-survey, downwind AMOG surface profile ascent Edison–Breckenridge ($\varepsilon - \varepsilon'$) and descent Breckenridge–Bodfish–Caliente ($\tau - \tau'$). Upwind profile visible top left. Planetary boundary layer (PBL) identified.

transect altitude level on the right and left sides, i.e., $U_{\mathrm{N_L}}(z)$ and $U_{N_R}(z)$. Gaussian distributions with half-widths of 1σ based on the values of $U_{\mathrm{N_L}}(x,z)$ and $U_{\mathrm{N_R}}(x,z)$ were formed for each transect altitude. The distribution was randomly sampled to populate $U_{\mathrm{N}}(x,z)$ and then interpolated as described above. Other variables were Monte Carlo-simulated in the same manner; i.e., a Gaussian distribution was calculated for the left and right portions of the data based on 1 standard deviation in the observations of the variable around its mean. Variables then were randomly sampled and interpolated. Specifically, Monte Carlo simulations also addressed C_{B} and C. Because instrumentation error is so much less than spatial and temporal variability, Monte Carlo simulation of C_{B} represents uncertainty in the source of the background (upwind) air, which could have some veering from the east or west coupled with convergence in the horizontal plane. One million Monte Carlo simulations were run for a flux uncertainty calculation.

3 Results

3.1 Profile data

Four vertical profiles (surface and airborne) were collected to understand PBL evolution during the survey (2 h) and across the survey domain spanning the experiment. Primary changes were development of near-surface winds and a slight increase in the PBL. AMOG Surveyor and AJAX collected pre-survey intercomparison vertical profiles ~ 30 km north of the Kern Fields between the small town of Delano on the SJV floor (100 m) up to a meadow (2058 m) above Shirley Meadows on a ridge of the Greenhorn Mountains in the Sierra Nevada range (Fig. 3). This profile spans a wide range of topography, from grasslands on rolling hills to tall pine trees near Alta Sierra; see Supplement Fig. S5 for surface images along the profile. AMOG Surveyor also conducted a post-survey, downwind vertical atmospheric profile to 1800 m a.s.l. Approximately 15 min of data were collected in an open (200–300 m) field above Shirley Meadows that was fairly exposed with only thin stands of pine trees on terrain falling steeply off to both sides. The wind direction and speeds for the field were consistent with winds at Alta Sierra, several hundred meters below, where AMOG was surrounded by tall trees. The field was above the top of the AJAX profile.

AMOG Surveyor's vertical ascent was collected before the AJAX profile to enable concurrent AMOG and AJAX data collection for the Kern Fields. The AMOG Surveyor ascent and descent were from 18:48 to 21:09 (20:08 UTC at crest), while AJAX flew a descent pattern from 20:58 to 21:04 UTC. AMOG Surveyor's descent was shortened to ~ 1000 m altitude (Glenville, CA) to allow AMOG to reach the Kern Fields nearly concurrent with AJAX and GOSAT.

AMOG and AJAX profile data overlapped between 500 and 2000 m. There was very good agreement between the two platforms for CO_2 and CH_4 for altitudes between 1.55 and 2 km (Fig. 4a and b), 99.9 and 99.7 %. AMOG and AJAX

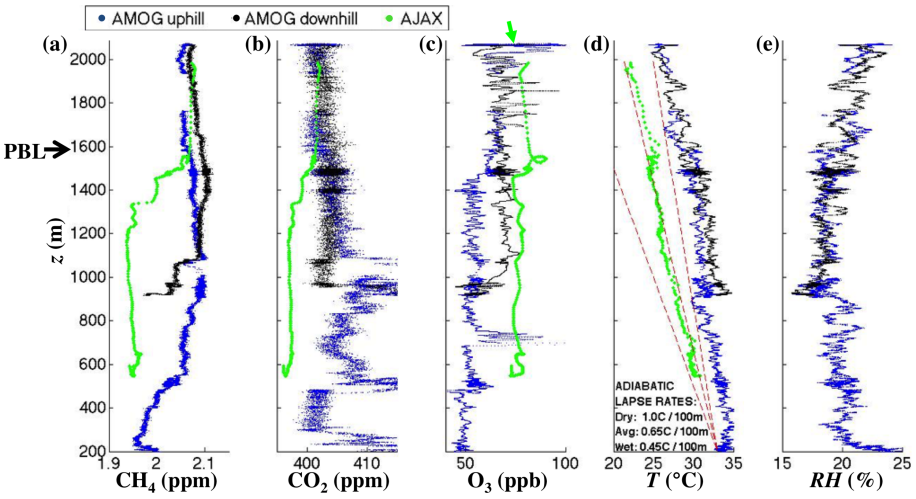

Figure 4. Surface altitude (z) above mean sea level profiles for west–east Delano–Alta Sierra transect (Fig. 3a, $\alpha - \alpha'$) for AMOG and AJAX **(a)** methane (CH_4), **(b)** carbon dioxide (CO_2), **(c)** ozone (O_3), **(d)** temperature (T), and **(e)** relative humidity (RH). Also shown in **(d)** are the dry, average, and wet adiabatic lapse rates. Data key in panel; planetary boundary layer (PBL) labeled. Green arrow shows extrapolation of AJAX trend to Shirley Meadows altitude (2058 m).

CH_4 concentrations decreased notably from the well-mixed PBL to the near-surface layer, from ∼ 2.07 ppm (500–750 m) to ∼ 1.93 ppm (250–300 m). AJAX also showed a decrease in CO_2 from 403 ppm to below 400 ppm. The CO_2 decrease was consistent with a shift to agricultural air, where CO_2 vegetative uptake reduces CO_2 concentrations. The PBL grew from 600 to 900 m between AMOG's ascent and descent and then to 1500 m by the time of AJAX's descent based on the CH_4, CO_2, and O_3 data.

The PBL was identified at ∼ 1580–1600 m based on both surface and airborne RH and T vertical profiles. Winds were not useful for deriving the location of the PBL. Diurnal heating is apparent between the two AMOG Surveyor T profiles but does not change the lapse rate. Because AJAX flies above the surface where AMOG collects data, AJAX temperatures are lower. In the lower atmosphere, the lapse rate was 6.9 °C km^{-1} for AJAX between 500 and 900 m, while the AMOG lapse rate from 200 to 900 m was a similar 5.6 °C km^{-1}. Between 950 and the top of the PBL, AMOG lapse rates were much shallower, 2.5 °C km^{-1}, with a jump in temperature at 900 m. Above the PBL, the AMOG-measured lapse rate was 3.5 °C km^{-1}, close to the wet adiabatic lapse rate (Fig. 4d).

Above the PBL, O_3 concentrations between AMOG and AJAX were ∼ 20 ppb different, although the AMOG and AJAX profile slopes (dO_3 / dz) were the same. If the trend in AJAX $O_3(z)$ from 1600 to 1850 m is extended to $z = 2058$ m (Fig. 3c, green arrow), there is agreement with AMOG Shirley Meadows (open field) O_3 concentrations. This similar slope but different absolute value could indicate O_3 loss as it diffused down through the pine canopy to the surface (and AMOG). Tall pine trees (30+ m) dominate above ∼ 1700, except for Shirley Meadows, where, as noted, there was good agreement. For $900 < z < 1400$ m, AJAX–AMOG agreement was better for the descent, which was closer in time to AJAX than the ascent. This shift likely was associated with formation of the daytime PBL.

In this upwind profile, AJAX observed elevated O_3 that was well mixed down to 500 m, while earlier AMOG showed well-mixed O_3 down to only 1100 m. There also was a small (∼ 10 ppb) O_3 enhancement at the top of the PBL in both the airborne and surface profiles. The highest O_3 concentrations were observed by AMOG in Shirley Meadows, where visibility was low due to smoke aerosols from the Rough Fire (NASA, 2015). Air above the PBL was more humid than elsewhere in the profile, except for the lowest 50 m above the valley floor, which was enriched in CH_4, CO_2, and RH, possibly from nocturnal accumulation and agriculture including irrigation RH inputs. There were thin layers in the atmosphere that suggest remnant structures from the prior day. For example, at ∼ 550 m the air changed character, with a jump in CO_2 by ∼ 10 ppm and of O_3 by ∼ 10 ppb, and a decrease in the CH_4 altitude gradient (dCH_4 / dz).

Air was more polluted at greater altitude above the PBL in the upwind (Delano–Alta Sierra) profile for O_3 for both platforms with air 10–20 ppb greater than in the PBL. Additionally, AJAX CH_4 and CO_2 were significantly higher above the PBL. The AMOG CH_4 and CO_2 data are less clear, presumably because AMOG data were prior to the disappearance of the nocturnal, stably stratified PBL. This was consistent with visual observations of haze by AMOG from Shirley Meadows as well as by the AJAX pilot. Additionally, air above the PBL was more humid.

A downwind ascent profile in the SJV was collected from Edison, CA, to the high flanks of Breckenridge Mountain, followed by a descent behind Breckenridge Mountain to

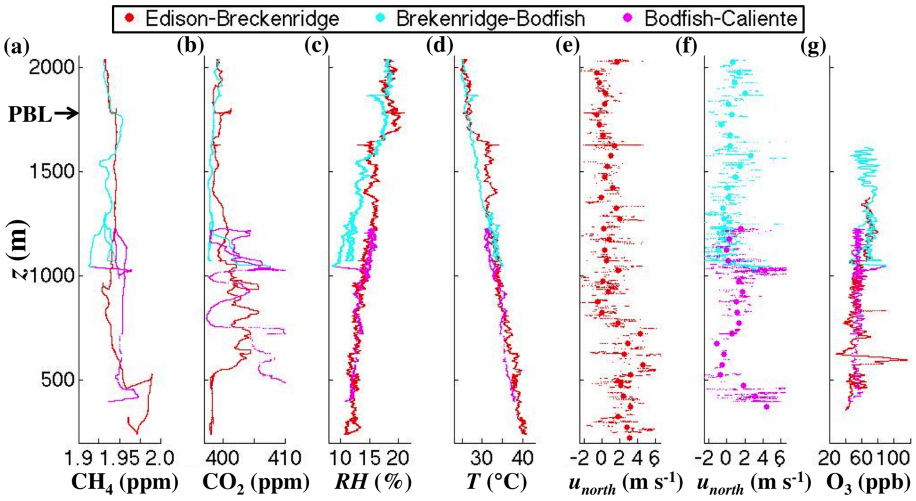

Figure 5. Surface altitude (z) above sea level profiles for Edison–Breckenridge ascent (red) and descent (blue) to Bodfish and then Caliente profile (magenta) (Fig. 3b) for AMOG Surveyor **(a)** methane (CH_4), **(b)** carbon dioxide (CO_2), **(c)** relative humidity (RH), **(d)** temperature (T), north wind (U_{north}) for **(e)** ascent and **(f)** descent (dots show 50 m altitude-binned averaged), and **(g)** ozone (O_3). Planetary boundary layer (PBL) labeled.

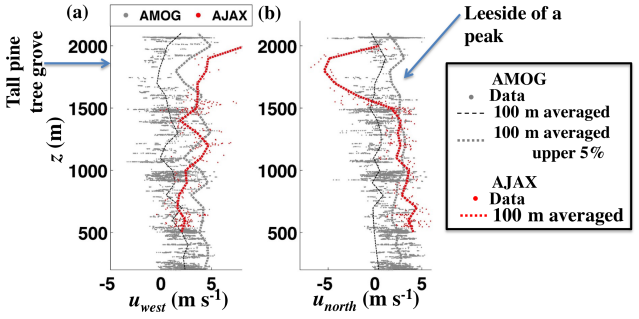

Figure 6. Altitude (z) profiles for **(a)** west (upslope) and **(b)** north (cross slope) wind components from AMOG and AJAX for overlapping altitudes of the Delano–Alta Sierra transit (Fig. 3, $\alpha - \alpha'$), 100 m altitude rolling-averaged data for AJAX, AMOG, and AMOG upper 5 % of winds. Data key in figure.

Caliente, CA, through the tiny town of Bodfish (Fig. 3b). This descent was separated from the SJV by a ridge and includes dryer, clean air that is representative of air from around Lake Isabella, a fairly isolated mountain valley. The downwind profile was collected quasi-Lagrangian in that the time separating the two profiles (about 4 h) is comparable to the transport time (75 km at a mean wind speed of 4 m s^{-1}, implying 5 h for transport). Thus, the downwind profile was for close to the same air. Over these hours, there was some additional PBL growth, ∼ 100 m growth to ∼ 1675 m, with highly uniform CH_4 between 1000 m and the top of the PBL (Fig. 5a). Thus, the PBL remained fairly stable over the course of the study. Air in both the upper PBL and above was cleaner with lower humidity and CH_4 concentrations. Unfortunately, the O_3 analyzer overheated during the ascent and resumed collecting data on the descent at ∼ 1500 m.

Direct comparison between AMOG and AJAX winds is inappropriate because AMOG winds are affected strongly by obstacles including hills, trees, and buildings. However, in many instances, terrain is open or gently rolling hills, and there tend to be regions of stronger winds that we propose are representative of free-atmosphere winds. AMOG data were altitude-binned, and the strongest winds in each bin were compared with AJAX (Fig. 6). Agreement is generally good (within 15–20 %) between the upper 5 % of AMOG cross-slope (west) winds in each altitude-averaged band (Fig. 6a). For the upslope wind (north) agreement is better (within 5–10 %) for a larger range of altitudes (Fig. 6b). This allows fusions of the upper 5 % of AMOG winds with AJAX winds. Over the full altitude range, the median differences were 38 and 27 % for the north and east wind components, respectively; see Supplement Fig. S7 for the altitude variation in the agreement.

3.2 Kern Fields and Bakersfield greenhouse gas emissions

3.2.1 Methane

On 19 August 2015, winds over the Kern Fields were prevailing (northwesterly) and fairly strong (∼ 3 m s^{-1}) on the ground and somewhat stronger aloft (Fig. 7). Potential plumes from the only nearby upwind dairy (Fig. 7a, white arrow) were directed by winds to pass to the west of the oil fields; agricultural fields in this part of the SJV are dry. As a result, surface topography like the Kern River Bluffs imposed only small wind modification at the surface and at alti-

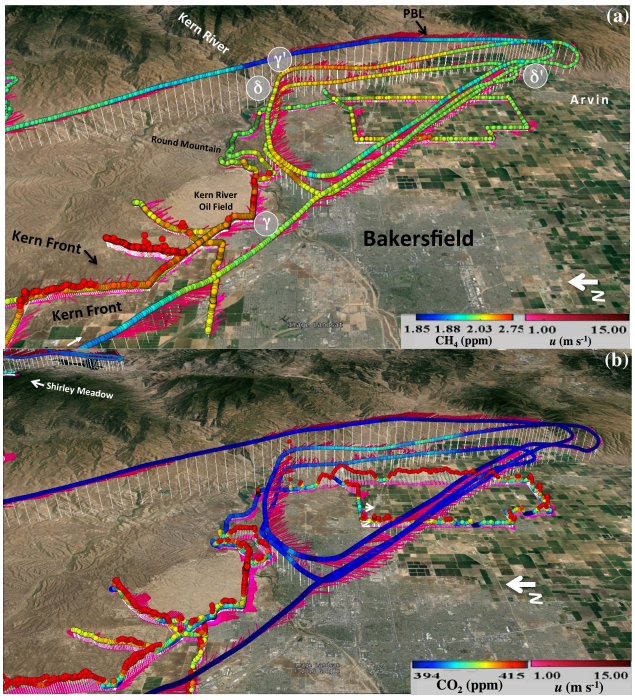

Figure 7. Combined AJAX and AMOG winds and in situ **(a)** methane (CH_4) and **(b)** carbon dioxide (CO_2) for the Kern Fields on 19 August 2015 for prevailing wind conditions. White arrow to the west of Kern Front oil field shows location of nearby dairy. Greek letters identify two downwind curtains. Red star in **(b)** locates origin for transect γ–γ'. Data keys in figure.

tude. Southeast of Bakersfield, winds veered to westerlies towards passes in the Sierra Nevada that connect to the Mojave Desert. The downwind survey included two plume transits on agricultural roads with negligible to no traffic. These transits clearly show the plume's eastward drift, passing to the north of the small town of Arvin, CA.

The background CH_4 plane $C_B(x,z)$ was extracted from the CH_4 data outside the plume – $C_{BL}(z)$ and $C_{BR}(z)$ (see Eq. 2) – immediately downwind of the Kern Fields (transect γ–γn). C_B showed a slight increase towards the east of ~ 20 ppb (Supplement Fig. S6a). The normal wind (U_N) was fairly uniform across the data plane, including downwind of the canyon (Fig. 8e). Thus, the CH_4 flux ($Q_{CH_4}(x,z)$ shows similar spatial patterns to CH_4'(x,z). Emissions from the Kern Fields were dominated by a large, focused CH_4 plume (or group of plumes) in the core of a much broader, dispersed, and poorly defined plume. This structure is evident in both surface AMOG data and in the lowest AJAX altitude for plane γ–γn, with both showing the strongest peak at $x = 4.5$ km (Fig. 8b, dashed lines). Total estimated emissions (E) were $63.5 \pm 50\,\%$ Mol s^{-1} (equivalent to 32 Gg yr^{-1}). Uncertainty is from the Monte Carlo simulations, described in Sect. 2.5.

Within the plume, concentrations are elevated at 1200 m altitude relative to 500 m and the surface, indicating buoyant rise. Additional evidence for buoyant rise is provided by two small plumes at $x \sim 1.7$ and 5.7 km that were centered at the top of the PBL but were not also observed in surface and mid-altitude data. The upper AJAX flight line was several hundred meters below the top of the PBL (at ~ 1580 m, Fig. 4), which constrains the main plume and was centered vertically in the PBL. Concentrations above the PBL were determined from AJAX descent and ascent data (Fig. 4), in agreement with AMOG data above the PBL. These observations show that the plume was not well mixed across the PBL. Another important feature is that the upper-altitude clean-air intrusion at $x \sim 6.5$ km lies downwind of the north–south canyon to the southeast of Round Mountain (Figs. 8b, 7a for location). This intrusion does not penetrate down to 500 m and represents a downslope airflow of cleaner upper-level air.

For comparison, a recent bottom-up estimate of CH_4 emissions based on production data for the Kern Fields estimated 10–40 Gg CH_4 yr^{-1} (68 % confidence level), by combining oil and gas production data with US-EPA emissions factors for associated wells (Jeong et al., 2014). Other CH_4 sources are unlikely to confuse this interpretation as petroleum system emissions are ~ 20 times larger than estimated nearby livestock and landfill CH_4 emissions of ~ 2.3 and 1.4 Gg yr^{-1}, respectively (Calgem, 2014).

3.2.2 Carbon dioxide

Background CO_2 for data curtain γ–γ' (Supplement Fig. S6b) was highly uniform. Given the strong crosswinds and care taken to avoid trailing other vehicles on the low-trafficked China Loop Road, these data passed quality review – CO_2 exhaust contamination manifests as a dramatic increase in the standard deviation whenever AMOG intersects a vehicle exhaust's turbulent plume. There was a shallow CO_2 layer constrained to the lower 100 to 200 m with ~ 10 ppm enhancement (Fig. 9a), also observed in the CO_2 vertical profile (Fig. 4b), a layer that was characterized by elevated relative humidity. Further evidence that these broad spatial CO_2 emissions are real is from the spatial similarity to CO_2 enhancements in the lowest AJAX flight data (Fig. 9c). For example, the surface CO_2 plume was strongest at $x \sim 4.5$ km in AMOG and AJAX data. The broad spatial extent of these emissions, similar to the broad CH_4 emissions, suggests a relationship to field-scale (engineering or geological) processes. Overall CO_2 emissions were $1730 \pm 50\,\%$ Mol s^{-1} (equivalent to 2.4 ± 1.2 Tg yr^{-1}).

There was a strong CO_2 anomaly in a focused plume at $x = 5$ km and $z = 1$ km. This plume likely relates to the two cogeneration power plants located in the Kern River oil field. Further support for this interpretation is its co-location with a similarly focused CH_4 plume at the same location. This power-plant-related feature is a persistent feature that has been observed in other surveys (Leifer, unpublished data). The upper clean-air intrusion in the CH_4 data curtain also is

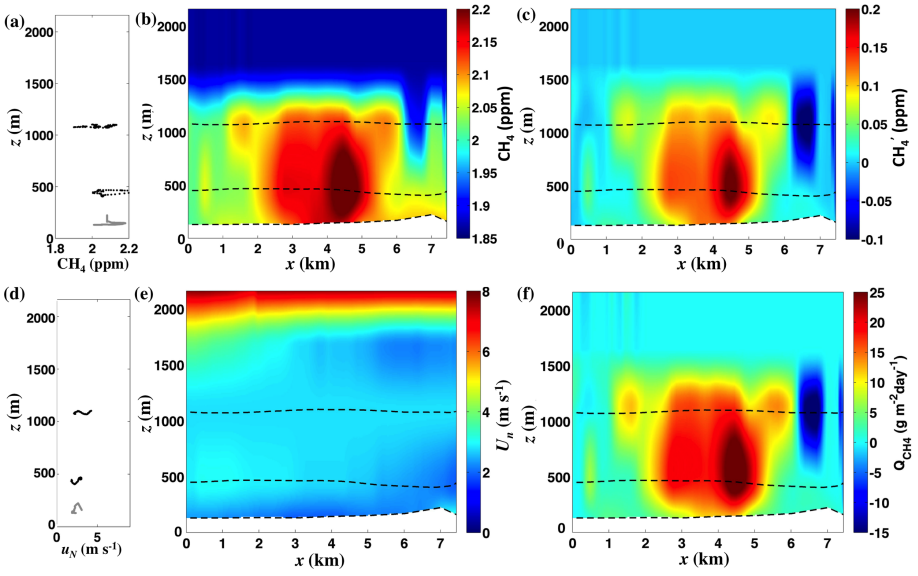

Figure 8. (a) Methane (CH_4) altitude (z) profiles for 19 August 2015 for AJAX (black) and AMOG (gray) data. **(b)** Interpolated, fused AJAX and AMOG CH_4 data with respect to lateral east distance (x) relative to 119.0023° W, 35.3842° N for data plane γ–γ' (Fig. 7). Dashed lines show data locations. **(c)** CH_4 anomaly (CH_4') relative to the background data plane (Supplement Fig. S6a). **(d)** Vertical normal wind profile (U_N) from AJAX (black) and AMOG (gray) data during ascent/descent; **(e)** interpolated, fused U_N; and **(f)** CH_4 flux (Q_{CH_4}) for the Kern Fields. Data key in panels.

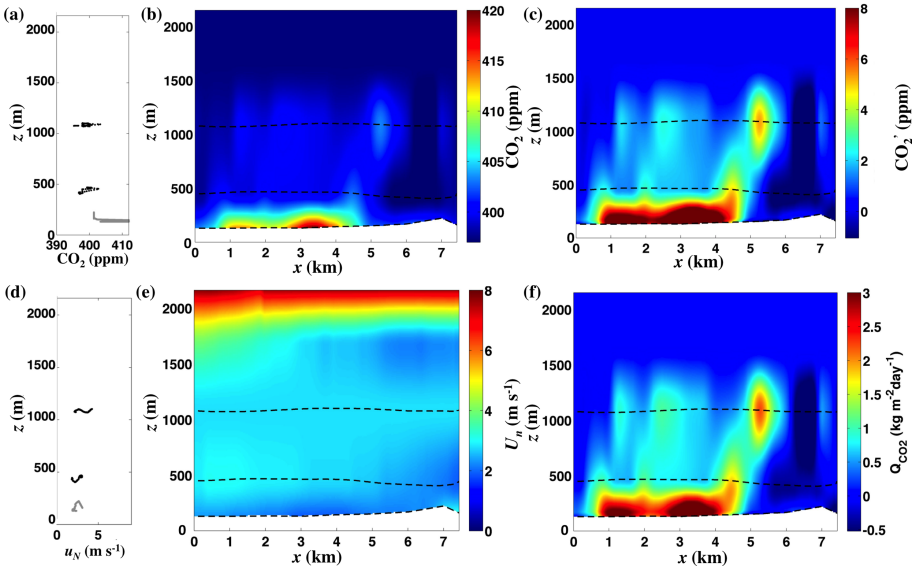

Figure 9. (a) Vertical carbon dioxide (CO_2) altitude (z) profile data for 19 August 2015 for AJAX (black) and AMOG (gray) data. **(b)** Interpolated, fused AJAX and AMOG CO_2 data curtain with respect to lateral east distance, x, relative to 119.0023° W, 35.3842° N for curtain γ–γ' (Fig. 7b). Dashed lines show data locations. **(c)** CO_2 anomaly (CO_2'). **(e)** Vertical normal wind profile (U_N). **(e)** Interpolated, fused U_N and **(f)** CO_2 flux (Q_{CO2}) for the Kern River and Kern Front oil fields for 19 August 2015. Data key in panels.

apparent in the CO_2 data (Fig. 9b), in front of the north–south canyon to the southeast of Round Mountain (Fig. 7).

Based on a reservoir $CO_2 : CH_4$ gas ratio of 92.2 % : 1.7 % (Lillis et al., 2008) and 32 Gg yr^{-1} CH_4 emissions, the Kern Fields CO_2 emissions were predicted to be 1.8 Tg yr^{-1}, which is fairly consistent with the directly derived emissions of 2.4 Tg yr^{-1}. Both these values are somewhat lower than the inventory for the cogeneration plants in Kern River oil field, 3.1 Tg yr^{-1} (CARB, 2016). The disagreement with inventory likely arises from the cogeneration plant only being active some of the time, confirmed by data from the GOSAT-COMEX campaign.

4 Discussion

4.1 Experimental design and real-time visualization

Ideally, GCE airborne and surface data are collected first upwind and then downwind. However, AJAX airborne data are not collected in a Lagrangian sense as would be necessary for a slower, less maneuverable airborne platform thanks to its extreme speed and maneuverability. This allows collection of near-snapshot (~ 30 min) data. Slower, AMOG surface data were collected in a quasi-Lagrangian sense, reducing the likelihood of confounding interference in the study area from non-FFI SJV inputs due to wind shifts after the pre-survey (for non-nominal winds the collection is aborted). Given the AJAX–AMOG speed difference, concurrent surface and airborne data could not be collected both upwind and downwind, and thus, concurrency was prioritized for downwind. For flight efficiency and to provide downwind concurrency with AMOG, AJAX flew a triangle that allowed AJAX to complete transects at three altitudes in close to AMOG's upwind–downwind survey time.

After the Kern Fields survey, AJAX returned to base, while AMOG collected additional surface data, exploring the fate of emissions from the Kern Fields. The word "exploring" is significant, as real-time visualization of winds, CH_4, and O_3 guided the downwind surveying. Data were collected to test the hypothesis that there was a relationship between wind strength and the specific outflow path from the SJV to Mojave Desert – specifically, that more northerly passes, which require greater wind veering from the prevailing direction, are preferred at lower winds speeds. The AMOG survey first confirmed that outflow was not up the Kern River Valley and then collected a downwind vertical profile into the Sierra Nevada to search for outflow through a pass near Breckenridge Mountain. After confirming its absence, AMOG then investigated in the Tehachapi Pass, where the outflow was identified. Thus, on 19 August 2015, when winds were strong, the outflow was by the most direct pathway – the Tehachapi Pass.

4.2 Experimental design and uncertainty reduction

The experimental design reduced uncertainty by characterizing the PBL through surface and airborne data fusion so that a well-mixed PBL is not required. Note that, for a well-mixed PBL, surface–airborne data fusion does not reduce uncertainty. The benefit arises for a not-well-mixed PBL where a significant fraction of the plume mass lies below the lowest altitude at which the airplane can fly. In such cases, surface data inclusion adds information to the PBL characterization. For example, flights can face airspace restrictions in cities, during airport approaches, in military airspace, and/or for safety.

Aerial survey altitudes were designed to span from near the top of the PBL to as low as permissible and include an intermediate level (0.5, 1, 1.2 km). Thus, surface data added information on the lowest third of the 1.6 km thick PBL. This lower portion of the PBL is more important on days when the PBL is shallower.

Observations showed that the well-mixed PBL assumption was poor as far as 10–20 km downwind. One solution is to collect data even further downwind, where the PBL should be better mixed (White et al., 1976); however, secondary (potentially uncharacterized) sources downwind of the study area and upwind of the downwind data plane add confounding anomalies. Also, wind flow complexity can lead to transport orthogonal to the overall downwind direction, leading to flux leakage out of the plume. The likelihood of plume loss increases over greater distances. And finally, as the PBL evolves with time, it imposes an evolving structure on the wind and concentration vertical profiles, which also challenge the well-mixed PBL assumption – particularly if transport to the downwind plane requires hours.

The in situ analyzers record concentration and winds with very high accuracy, albeit only at a single location and time. Thus, in situ uncertainty arises mostly from inadequate characterization of temporal variability and spatial heterogeneity in winds and emissions over the survey time period. The best strategy is to minimize study time; however, there is a necessary tradeoff between spatial resolution and study time. AJAX collects data quickly, allowing survey completion within far less than typical atmospheric change timescales. Similarly, the surface survey route was designed to minimize collection time, primarily on rural/agricultural roads carefully selected to avoid traffic congestion and traffic lights. The surface survey requires ~ 90 min to complete and is conducted quasi-Lagrangian.

GCE treats uncertainty explicitly, allowing improvements in the data collection strategy to reduce uncertainty. For example, the east–west downwind transect was lengthened from earlier data collections to characterize background concentrations better. GCE also does not require an a priori emission distribution and thus explicitly incorporates emissions from super-emitters, normal emitters, and distributed sources, improving robustness of the findings. In contrast, inversion models require a reasonable spatial a priori emission distribution and the ability to model transport across the study domain. However, complex wind flows from fine-scale topographic structures, as observed for the Kern Fields, challenge transport modeling.

4.3 Profile intercomparison

This study leveraged terrain to provide profile information with a surface mobile platform, which was compared with airborne data. In this study, the two were combined to provide more complete coverage of the atmosphere than a single platform could, at a fraction of the cost (not to mention logistical complexity) of having two airborne platforms. Whereas

the approach worked well in the San Joaquin Valley, further research is needed to confirm its utility in other settings.

Above the PBL, there was excellent agreement between surface and airborne concentration profile data, while concentration profiles within the PBL show significant differences between the two profiles, likely related to air mass shifts and diurnal heating during the time between the profiles (Fig. 4). Winds above the PBL were in poor agreement, with the north component in the opposite direction (Fig. 6). Underlying this discrepancy was a mountain peak, which clearly caused large-scale alterations in the wind flow field.

Within the PBL, agreement between unfiltered surface AMOG winds and AJAX winds was poor, unsurprising because surface winds are strongly affected by obstacles. However, by filtering AMOG winds (collected 3 m above the surface) for the strongest 5 %, agreement was within 15–20 % for the along-slope – i.e., north – winds and better for upslope winds (west). Specific exceptions were when AMOG was in a dense grove of pines, and when AJAX flew behind into the lee of a mountain peak. Surface winds are modulated by a wide range of surface factors, including trees, steep hills and hillocks, steep slopes, rolling hills, and structures (Supplement Fig. S5). However, a combination of gusts (among thin wooded terrain on steep slopes) and the limited spatial extent of most obstacles underlies the agreement between the filtered AMOG and AJAX wind profiles. Agreement is better for the upper portions of the PBL (within 10–20 %), where Sierra Nevada slopes are steeper. In contrast, the slope lower in the PBL is gentle, and surface boundary layer effects are more pronounced, biasing wind speeds slower.

The wind orientation to the slope affects the comparison because topography imposes wind-field structure at large and small scales. Where winds advect air upslope, transport incorporates a non-negligible vertical component that is missed by the 2-D sonic anemometer used in the study reported here. Currently, AMOG measures 3-D winds, as does AJAX.

Some of the discrepancy between AMOG and AJAX wind profiles could have arisen from temporal changes between the two profiles; however, this is unlikely for two reasons. First, the top of the PBL was identified four times over the course of the study and remained stable within 100 m across the domain. Second, surface wind observations remained relatively constant after the mid-morning shift to daytime conditions (breakup of nocturnal stratification). However, the poor agreement between AJAX and AMOG vertical concentration profiles within the PBL suggests significant air mass shifts – highlighting the need for better concurrence.

4.4 GHG FFI emissions

Emissions for the Kern Fields were estimated at $32 \pm 16\,\mathrm{Gg\,CH_4\,yr^{-1}}$, with CH_4 emissions $\sim 20\,\%$ above EPA inventories, and $2.4 \pm 1.2\,\mathrm{Tg\,CO_2\,yr^{-1}}$. The broad CO_2 plume suggests emissions from the geologic reservoir – likely along the same pathways associated with CH_4 leakage – in addition to the focused and not continuous emissions from the cogeneration power plants. On China Loop Road (where the CO_2 surface plume was transected), strong crosswinds and light traffic would have prevented significant vehicular CO_2 contamination. Additionally there are no upwind (non-oil-field) roads, only the foothills of the Sierra Nevada.

For comparison, a recent bottom-up estimate of CH_4 emissions from the Kern Fields estimated $25 \pm 15\,\mathrm{Gg\,CH_4\,yr^{-1}}$ by combining oil and gas production data with emissions factors for associated wells used by US-EPA (Jeong et al., 2014); i.e., 19 August 2015 CH_4 emissions were a third above inventories. The derived flux lies within the inventory uncertainty but is higher, consistent with a recent metastudy of field studies of FFI production emissions, which showed significant underestimation in the EPA budget (Brandt et al., 2014; Miller et al., 2013). A number of factors likely play a role, including the age of the Kern River oil field (over a century); production factors (steam injection); shallowness of the reservoir (< 300 m); location in a tectonically active area, which creates alternate migration pathways from the reservoir (Leifer et al., 2013); and the recent expansion of the number of wells in the Kern Front oil field (from Google Earth timeline imagery). Many of these factors are common to other production fields in California, the US, and globally. Given the importance of FFI to the overall budget, even small underestimation could be highly significant. Thus, this uncertainty highlights the need for improved measurement tools to reduce the significant uncertainty in the CH_4 budget and for satellite measurement validation, particularly for complex terrain and in the source's near field.

5 Conclusions

This study showed how to combine airborne and surface in situ data to improve emissions derivation, and it demonstrated the novel use of topography to characterize vertical atmospheric structure with a surface mobile platform. Given that mountains cover a significant fraction of the earth's land surface, further research should be undertaken to confirm that this approach applies in other settings. Data showed the PBL was not well mixed, even 10–20 km downwind, highlighting the importance of the direct flux quantification approach. Direct quantification does not require accurate modeling of winds across complex terrain, but it does require interpolation and data modeling to identify the background.

Appendix A: Table of nomenclature

	Units	Description
AJAX	(–)	Alpha Jet Atmospheric eXperiment
AMOG	(–)	AutoMObile trace Gas
Bbl	(–)	Barrel (of oil); 1 bbl = 6.38 m^3
COMEX	(–)	CO_2 and MEthane eXperiment
EOR	(–)	Enhanced oil recovery (techniques)
EPA	(–)	Environmental Protection Agency
GCE	(–)	GOSAT COMEX Experiment
GHG	(–)	Greenhouse gas
GOSAT	(–)	Greenhouse gases Observing SATellite
PBL	(–)	Planetary boundary layer
SJV	(–)	San Joaquin Valley
Tg		Terragram (10^{12} g)
UTC	(–)	Universal time
$C'(x,z)$	(ppm)	Concentration anomaly (above C_B)
$C(x,z)$	(ppm)	Concentration
$C_B(x,z)$	(ppm)	Background concentration – outside plume
$C_{BL}(z)$	(ppm)	Background concentration profile – left side of profile
$C_{BR}(z)$	(ppm)	Background concentration profile – right side of profile
E	(mol s^{-1})	Emission source strength
$k(z)$	(mol ppm^{-1})	Conversion factor from the ideal gas law
N'	(mol cm^{-3})	Molar mass anomaly
$Q(x,z)$	(mol m^{-2} s^{-1})	Flux through the data plane
R^2	(–)	Correlation coefficient
RH	(%)	Relative humidity
T	(°C)	Temperature
$U_N(x,z)$	(m s^{-1})	Winds normal to the data plane, a function of (x,z)
U_{north}	(m s^{-1})	North wind component
U_{west}	(m s^{-1})	West wind component
x	(m)	Lateral distance – approximately cross-wind
x_L	(m)	Left half of the transect ($x < x_{max}/2$)
x_{max}	(m)	Length of a transect
x_R	(m)	Right half of the transect ($x > x_{max}/2$)
y	(m)	Lateral distance – approximately co-wind
z	(m)	Altitude
$\Phi_L(C)$	(–)	Concentration probability distribution for left side of transect
$\Phi_R(C)$	(–)	Concentration probability distribution for right side of transect
$\Phi_P(C)$	(–)	Concentration probability distribution for the plume
$\Phi_B(C)$	(–)	Concentration probability distribution for the background
α, α'	(–)	Designation for Delano–Alta Sierra surface transect
$\varepsilon, \varepsilon'$	(–)	Designation for Edison–Breckenridge Mtn. surface transect
τ, τ'	(–)	Designation for Breckenridge–Caliente surface transect
β, β', β_1'	(–)	Designation for Wasco–Granite surface transect
γ, γ'	(–)	Designation for Oildale–Oil City surface and airborne transects
δ, δ'	(–)	Designation for Ming Park–Arvin surface and airborne transects

Data availability. Data can be obtained by contacting the corresponding author, Ira Leifer (ira.leifer@bubbleology.com).

The Supplement related to this article is available online at https://doi.org/10.5194/amt-11-1689-2018-supplement.

Author contributions. IL prepared the manuscript with input from all co-authors. CM prepared figures and conducted data analysis. MF helped prepare the emissions budgets. JF helped with AMOG data collection. LI, JM, JMR, TT, and EY are part of the AJAX team and worked to collect and analyze AJAX data.

Competing interests. The authors declare that they have no conflict of interest.

Acknowledgements. We thank the NASA Earth Science Division Research and Analysis Program, grant NNX13AM21G. Marc. L. Fischer was supported by a grant from the California Energy Commission's Natural Gas Research Program to the Lawrence Berkeley National Laboratory under contract DE-AC02-36605CH11231. AJAX data were collected under the AJAX project, which acknowledges the partnership of H211, LLC, and funding from the Ames Research Center. Funding for Josette. E. Marrero, Ju-Mee Ryoo, and Tomoaki Tanaka was provided by the NASA Postdoctoral Program.

Edited by: Fred Prata
Reviewed by: two anonymous referees

References

Allen, G.: Biogeochemistry: Rebalancing the global methane budget, Nature, 538, 46–48, 2016.

State of the Air: Chicago, IL, American Lung Association: 157 pp., www.lung.org/assets/documents/healthy-air/state-of-the-air/sota-2016-full.pdf (last access: March 2018), 2016.

Bao, J. W., Michelson, S. A., Persson, P. O. G., Djalalova, I. V., and Wilczak, J. M.: Observed and WRF-simulated low-level winds in a high-ozone episode during the Central California Ozone Study, J. Appl. Meteorol. Clim., 47, 2372–2394, 2008.

Boucouvala, D. and Bornstein, R.: Analysis of transport patterns during an SCOS97-NARSTO episode, Atmos. Environment, 37, Supplement 2, 73–94, 2003.

Brandt, A. R., Heath, G. A., Kort, E. A., O'Sullivan, F., Pétron, G., Jordaan, S. M., Tans, P., Wilcox, J., Gopstein, A. M., Arent, D., Wofsy, S., Brown, N. J., Bradley, R., Stucky, G. D., Eardley, D., and Harriss, R.: Methane leaks from North American natural gas systems, Science, 343, 733–735, 2014.

Calgem: California Greenhouse Gas Emissions Measurement (CALGEM) Project. DOE, http://calgem.lbl.gov/, 2014.

CARB: Facility GHG Emissions Visualization and Analysis Tool: 2008–2014, Calfornia Environmental Protection Agency, Air Resources Board, 2016.

Chen, H., Winderlich, J., Gerbig, C., Hoefer, A., Rella, C. W., Crosson, E. R., Van Pelt, A. D., Steinbach, J., Kolle, O., Beck, V., Daube, B. C., Gottlieb, E. W., Chow, V. Y., Santoni, G. W., and Wofsy, S. C.: High-accuracy continuous airborne measurements of greenhouse gases (CO_2 and CH_4) using the cavity ring-down spectroscopy (CRDS) technique, Atmos. Meas. Tech., 3, 375–386, https://doi.org/10.5194/amt-3-375-2010, 2010.

Dlugokencky, E. J., Nisbet, E. G., Fisher, R., and Lowry, D.: Global atmospheric methane: Budget, changes and dangers, Philos. T. R. Soc. A, 369, 2058–2072, 2011.

Dlugokencky, E. J., Crotwell, A., Masarie, K., White, J., Lang, P., and Crotwell, M.: NOAA Measurements of Long-lived Greenhouse Gases, Asia-Pacific GAW Greenhouse Gases, 6, 6–9, 2013.

EPA: 2013 Inventory of US greenhouse gas: Emissions and sinks: 1990–2011, Environmental Protection Agency, Washington DC, 457 pp., 2013.

EPA: 2017 Inventory of US greenhouse gas: Emissions and sinks: 1990–2015, Environmental Protection Agency, Washington DC430-P-17-001, 633 pp., 2017.

European Commission: Emission Database for Global Atmospheric Research (EDGAR), Joint Research Centre (JRC)/Netherlands Environmental Assessment Agency (PBL), 2010.

Farrell, P., Leifer, I., and Culling, D.: Transcontinental methane measurements: Part 1. A mobile surface platform for source investigations, Atmos. Environ., 74, 422–431, 2013.

Fernandez-Cortes, A., Cuezva, S., Alvarez-Gallego, M., Garcia-Anton, E., Pla, C., Benavente, D., Jurado, V., Saiz-Jimenez, C., and Sanchez-Moral, S.: Subterranean atmospheres may act as daily methane sinks, Nat. Commun., 6, 7003, 2015.

Gentner, D. R., Ford, T. B., Guha, A., Boulanger, K., Brioude, J., Angevine, W. M., de Gouw, J. A., Warneke, C., Gilman, J. B., Ryerson, T. B., Peischl, J., Meinardi, S., Blake, D. R., Atlas, E., Lonneman, W. A., Kleindienst, T. E., Beaver, M. R., Clair, J. M. St., Wennberg, P. O., VandenBoer, T. C., Markovic, M. Z., Murphy, J. G., Harley, R. A., and Goldstein, A. H.: Emissions of organic carbon and methane from petroleum and dairy operations in California's San Joaquin Valley, Atmos. Chem. Phys., 14, 4955–4978, https://doi.org/10.5194/acp-14-4955-2014, 2014.

Ghosh, A., Patra, P. K., Ishijima, K., Umezawa, T., Ito, A., Etheridge, D. M., Sugawara, S., Kawamura, K., Miller, J. B., Dlugokencky, E. J., Krummel, P. B., Fraser, P. J., Steele, L. P., Langenfelds, R. L., Trudinger, C. M., White, J. W. C., Vaughn, B., Saeki, T., Aoki, S., and Nakazawa, T.: Variations in global methane sources and sinks during 1910–2010, Atmos. Chem. Phys., 15, 2595–2612, https://doi.org/10.5194/acp-15-2595-2015, 2015.

Hamill, P., Iraci, L. T., Yates, E. L., Gore, W., Bui, T. P., Tanaka, T., and Loewenstein, M.: A new instrumented airborne platform for atmospheric research, B. Am. Meteorol. Soc., 97, 397–404, https://doi.org/10.1175/BAMS-D-14-00241.1, 2016.

IPCC: Climate Change 2007: Synthesis Report. Contribution of Working Groups I, II, and III to the Fourth Assessment Report of the Intergovernmental Panel on Climate Change, IPCC, Geneva, Switzerland, 104 pp., 2007.

IPCC: Working Group 1 Contribution to the IPCC Fifth Assessment Report Climate Change 2013 – The Physical Science Basis, International Panel on Climate Change, IPCC Secretariat, Geneva, Switzerland, 2216 pp., 2013.

Jeong, S., Zhao, C., Andrews, A. E., Bianco, L., Wilczak, J. M., and Fischer, M. L.: Seasonal variation of CH_4 emissions from central California, J. Geophys. Res., 117, D11306, https://doi.org/10.1029/2011jd016896, 2012.

Jeong, S., Hsu, Y.-K., Andrews, A. E., Bianco, L., Vaca, P., Wilczak, J. M., and Fischer, M.: Multi-tower measurement network estimate of California's methane emissions, J. Geophys. Res.-Atmos., 118, 11339–11351, https://doi.org/10.1002/jgrd.50854, 2013.

Jeong, S. S., Millstein, D., and Fischer, M. L.: Spatially explicit methane emissions from petroleum production and the natural gas system in California, Environ. Sci. Technol., 48, 5982–5990, 2014.

John, J. G., Fiore, A. M., Naik, V., Horowitz, L. W., and Dunne, J. P.: Climate versus emission drivers of methane lifetime against loss by tropospheric OH from 1860–2100, Atmos. Chem. Phys., 12, 12021–12036, https://doi.org/10.5194/acp-12-12021-2012, 2012.

Karion, A., Sweeney, C., Pétron, G., Frost, G., Michael Hardesty, R., Kofler, J., Miller, B. R., Newberger, T., Wolter, S., Banta, R., Brewer, A., Dlugokencky, E., Lang, P., Montzka, S. A., Schnell, R., Tans, P., Trainer, M., Zamora, R., and Conley, S.: Methane emissions estimate from airborne measurements over a western United States natural gas field, Geophys. Res. Lett., 40, 4393–4397, 2013.

Karlsdóttir, S. and Isaksen, I. S. A.: Changing methane lifetime: Possible cause for reduced growth, Geophys. Res. Lett., 27, 93–96, 2000.

Khalil, M. A. K. and Rasmussen, R. A.: The changing composition of the Earth's atmosphere, in: Composition, chemistry, and climate of the atmosphere, edited by: Singh, H. B., Van Nostrand Reinhold, New York, 1995.

Kirschke, S., Bousquet, P., Ciais, P., Saunois, M., Canadell, J. G., Dlugokencky, E. J., Bergamaschi, P., Bergmann, D., Blake, D. R., and Bruhwiler, L.: Three decades of global methane sources and sinks, Nat. Geosci., 6, 813–823, 2013.

Krautwurst, S., Gerilowski, K., Krings, T., Borchard, J., Bovensmann, H., Leifer, I., Fladeland, M. M., Koyler, R., Iraci, L. T., Luna, B., Thompson, D. R., Eastwood, M., Green, R., Jonsson, H. H., Vigil, S. A., and Tratt, D. M.: COMEX – Final Report: Scientific and Technical Assistance for the Deployment of a flexible airborne spectrometer system during CMAPExp and COMEX, IUP-COMEX-FR, 148 pp., 2016.

Krings, T., Gerilowski, K., Buchwitz, M., Reuter, M., Tretner, A., Erzinger, J., Heinze, D., Pflüger, U., Burrows, J. P., and Bovensmann, H.: MAMAP – a new spectrometer system for column-averaged methane and carbon dioxide observations from aircraft: retrieval algorithm and first inversions for point source emission rates, Atmos. Meas. Tech., 4, 1735–1758, https://doi.org/10.5194/amt-4-1735-2011, 2011.

LaFranchi, B. W., Pétron, G., Miller, J. B., Lehman, S. J., Andrews, A. E., Dlugokencky, E. J., Hall, B., Miller, B. R., Montzka, S. A., Neff, W., Novelli, P. C., Sweeney, C., Turnbull, J. C., Wolfe, D. E., Tans, P. P., Gurney, K. R., and Guilderson, T. P.: Constraints on emissions of carbon monoxide, methane, and a suite of hydrocarbons in the Colorado Front Range using observations of $^{14}CO_2$, Atmos. Chem. Phys., 13, 11101–11120, https://doi.org/10.5194/acp-13-11101-2013, 2013.

Lamb, B. K., McManus, J., Shorter, J., Kolb, C., Mosher, B., Harriss, R., Allwine, E., Blaha, D., Howard, T., Guenther, A., Lott, R., Siverson, R., Westburg, H., and Zimmerman, P.: Development of atmospheric tracer methods to measure methane emissions from natural gas facilities and urban areas, Environ. Sci. Technol., 29, 1468–1479, 1995.

Leen, J. B., Yu, X. Y., Gupta, M., Baer, D. S., Hubbe, J. M., Kluzek, C. D., Tomlinson, J. M., and Hubbell, M. R., 2nd: Fast in situ airborne measurement of ammonia using a mid-infrared off-axis ICOS spectrometer, Environ. Sci. Tech., 47, 10446–10453, 2013.

Leifer, I., Culling, D., Schneising, O., Farrell, P., Buchwitz, M., and Burrows, J.: Transcontinental methane measurements: Part 2. Mobile surface investigation of fossil fuel industrial fugitive emissions, Atmos. Environ., 74, 432–441, 2013.

Leifer, I., Melton, C., Manish, G., and Leen, B.: Mobile monitoring of methane leakage, Gases and Instrumentation, July/August 2014, 20–24, 2014.

Leifer, I., Melton, C., Frash, J., Fischer, M. L., Cui, X., Murray, J. J., and Green, D. S.: Fusion of mobile in situ and satellite remote sensing observations of chemical release emissions to improve disaster response, Frontiers in Science, 4, 1–14, 2016.

Lillis, P. G., Warden, A., Claypool, G. E., and Magoon, L. B.: Petroleum systems of the San Joaquin Basin Province – geochemical characteristics of gas types: Chapter 10, in: Petroleum systems and geologic assessment of oil and gas in the San Joaquin Basin Province, California, edited by: Scheirer, A. H., 1713-10, U. S. Geological Survey, Reston, VA, 2008.

McKain, K., Down, A., Raciti, S. M., Budney, J., Hutyra, L. R., Floerchinger, C., Herndon, S. C., Nehrkorn, T., Zahniser, M. S., Jackson, R. B., Phillips, N., and Wofsy, S. C.: Methane emissions from natural gas infrastructure and use in the urban region of Boston, Massachusetts, P. Natl. Acad. Sci. USA, 112, 1941–1946, https://doi.org/10.1073/pnas.1416261112, 2015.

Miller, S. M., Wofsy, S. C., Michalak, A. M., Kort, E. A., Andrews, A. E., Biraud, S. C., Dlugokencky, E. J., Eluszkiewicz, J., Fischer, M. L., Janssens-Maenhout, G., Miller, B. R., Miller, J. B., Montzka, S. A., Nehrkorn, T., and Sweeney, C.: Anthropogenic emissions of methane in the United States, P. Natl. Acad. Sci. USA, 110, 20018–20022, 2013.

NASA: https://www.nasa.gov/image-feature/goddard/wildfires-in-california-august-17-2015 (last access: 16 April 2017), 2015.

Nisbet, E. G., Dlugokencky, E. J., and Bousquet, P.: Methane on the rise – Again, Science, 343, 493–495, 2014.

Nisbet, E. G., Dlugokencky, E. J., Manning, M. R., Lowry, D., Fisher, R. E., France, J. L., Michel, S. E., Miller, J. B., White, J. W. C., Vaughn, B., Bousquet, P., Pyle, J. A., Warwick, N. J., Cain, M., Brownlow, R., Zazzeri, G., Lanoisellé, M., Manning, A. C., Gloor, E., Worthy, D. E. J., Brunke, E. G., Labuschagne, C., Wolff, E. W., and Ganesan, A. L.: Rising atmospheric methane: 2007–2014 growth and isotopic shift, Global Biogeochem. Cy., 30, 1356–1370, 2016.

Peischl, J., Ryerson, T. B., Brioude, J., Aikin, K. C., Andrews, A. E., Atlas, E., Blake, D., Daube, B. C., de Gouw, J. A., Dlugokencky, E., Frost, G. J., Gentner, D. R., Gilman, J. B., Goldstein, A. H., Harley, R. A., Holloway, J. S., Kofler, J., Kuster, W. C., Lang, P. M., Novelli, P. C., Santoni, G. W., Trainer, M., Wofsy, S. C., and Parrish, D. D.: Quantifying sources of methane using light alkanes in the Los Angeles

basin, California, J. Geophys. Res.-Atmos., 120, 2119–2139, https://doi.org/10.1002/2014JD022697, 2013.

Peischl, J., Ryerson, T. B., Aikin, K. C., de Gouw, J. A., Gilman, J. B., Holloway, J. S., Lerner, B. M., Nadkarni, R., Neuman, J. A., Nowak, J. B., Trainer, M., Warneke, C., and Parrish, D. D.: Quantifying atmospheric methane emissions from the Haynesville, Fayetteville, and northeastern Marcellus shale gas production regions, J. Geophys. Res.-Atmos., 120, 2119–2139, 2015.

Peischl, J., Karion, A., Sweeney, C., Kort, E. A., Smith, M., L,., Brandt, A. R., Yeskoo, T., Aikin, K. C., Conley, S. A., and Gvakharia, A.: Quantifying atmospheric methane emissions from oil and natural gas production in the Bakken shale region of North Dakota, J. Geophys. Res.-Atmos., 212, P. Natl. Acad. Sci. USA, 2016.

Pétron, G., Frost, G., Miller, B. R., Hirsch, A. I., Montzka, S. A., Karion, A., Trainer, M., Sweeney, C., Andrews, A. E., Miller, L., Kofler, J., Bar-Ilan, A., Dlugokencky, E. J., Patrick, L., Moore, C. T. J., Ryerson, T. B., Siso, C., Kolodzey, W., Lang, P. M., Conway, T., Novelli, P., Masarie, K., Hall, B., Guenther, D., Kitzis, D., Miller, J., Welsh, D., Wolfe, D., Neff, W., and Tans, P.: Hydrocarbon emissions characterization in the Colorado Front Range: A pilot study, J. Geophys. Res., 117, D04304, https://doi.org/10.1029/2011JD016360, 2012.

Rigby, M., Prinn, R. G., Fraser, P. J., Simmonds, P. G., Langenfelds, R. L., Huang, J., Cunnold, D. M., Steele, L. P., Krummel, P. B., Weiss, R. F., O'Doherty, S., Salameh, P. K., Wang, H. J., Harth, C. M., Mühle, J., and Porter, L. W.: Renewed growth of atmospheric methane, Geophys. Res. Lett., 35, L22805, https://doi.org/10.1029/2008GL036037, 2008.

Rigby, M., Montzka, S. A., Prinn, R. G., White, J. W. C., Young, D., O'Doherty, S., Lunt, M. F., Ganesan, A. L., Manning, A. J., Simmonds, P. G., Salameh, P. K., Harth, C. M., Mühle, J., Weiss, R. F., Fraser, P. J., Steele, L. P., Krummel, P. B., McCulloch, A., and Park, S.: Role of atmospheric oxidation in recent methane growth, P. Natl. Acad. Sci. USA, 114, 5373–5377, 2017.

Saunois, M., Bousquet, P., Poulter, B., Peregon, A., Ciais, P., Canadell, J. G., Dlugokencky, E. J., Etiope, G., Bastviken, D., Houweling, S., Janssens-Maenhout, G., Tubiello, F. N., Castaldi, S., Jackson, R. B., Alexe, M., Arora, V. K., Beerling, D. J., Bergamaschi, P., Blake, D. R., Brailsford, G., Brovkin, V., Bruhwiler, L., Crevoisier, C., Crill, P., Covey, K., Curry, C., Frankenberg, C., Gedney, N., Höglund-Isaksson, L., Ishizawa, M., Ito, A., Joos, F., Kim, H.-S., Kleinen, T., Krummel, P., Lamarque, J.-F., Langenfelds, R., Locatelli, R., Machida, T., Maksyutov, S., McDonald, K. C., Marshall, J., Melton, J. R., Morino, I., Naik, V., O'Doherty, S., Parmentier, F.-J. W., Patra, P. K., Peng, C., Peng, S., Peters, G. P., Pison, I., Prigent, C., Prinn, R., Ramonet, M., Riley, W. J., Saito, M., Santini, M., Schroeder, R., Simpson, I. J., Spahni, R., Steele, P., Takizawa, A., Thornton, B. F., Tian, H., Tohjima, Y., Viovy, N., Voulgarakis, A., van Weele, M., van der Werf, G. R., Weiss, R., Wiedinmyer, C., Wilton, D. J., Wiltshire, A., Worthy, D., Wunch, D., Xu, X., Yoshida, Y., Zhang, B., Zhang, Z., and Zhu, Q.: The global methane budget 2000–2012, Earth Syst. Sci. Data, 8, 697–751, https://doi.org/10.5194/essd-8-697-2016, 2016.

Saunois, M., Bousquet, P., Poulter, B., Peregon, A., Ciais, P., Canadell, J. G., Dlugokencky, E. J., Etiope, G., Bastviken, D., Houweling, S., Janssens-Maenhout, G., Tubiello, F. N., Castaldi, S., Jackson, R. B., Alexe, M., Arora, V. K., Beerling, D. J., Bergamaschi, P., Blake, D. R., Brailsford, G., Bruhwiler, L., Crevoisier, C., Crill, P., Covey, K., Frankenberg, C., Gedney, N., Höglund-Isaksson, L., Ishizawa, M., Ito, A., Joos, F., Kim, H.-S., Kleinen, T., Krummel, P., Lamarque, J.-F., Langenfelds, R., Locatelli, R., Machida, T., Maksyutov, S., Melton, J. R., Morino, I., Naik, V., O'Doherty, S., Parmentier, F.-J. W., Patra, P. K., Peng, C., Peng, S., Peters, G. P., Pison, I., Prinn, R., Ramonet, M., Riley, W. J., Saito, M., Santini, M., Schroeder, R., Simpson, I. J., Spahni, R., Takizawa, A., Thornton, B. F., Tian, H., Tohjima, Y., Viovy, N., Voulgarakis, A., Weiss, R., Wilton, D. J., Wiltshire, A., Worthy, D., Wunch, D., Xu, X., Yoshida, Y., Zhang, B., Zhang, Z., and Zhu, Q.: Variability and quasi-decadal changes in the methane budget over the period 2000–2012, Atmos. Chem. Phys., 17, 11135–11161, https://doi.org/10.5194/acp-17-11135-2017, 2017.

Schwietzke, S., Sherwood, O. A., Bruhwiler, L. M. P., Miller, J. B., Etiope, G., Dlugokencky, E. J., Michel, S. E., Arling, V. A., Vaughn, B. H., White, J. W. C., and Tans, P. P.: Upward revision of global fossil fuel methane emissions based on isotope database, Nature, 538, 88–91, 2016.

Simpson, I. J., Sulbaek Andersen, M. P., Meinardi, S., Bruhwiler, L., Blake, N. J., Helmig, D., Rowland, F. S., and Blake, D. R.: Long-term decline of global atmospheric ethane concentrations and implications for methane, Nature, 488, 490–494, 2012.

Smith, M. L., Kort, E. A., Karion, A., Sweeney, C., Herndon, S. C., and Yacovitch, T. I.: Airborne ethane observations in the Barnett Shale: Quantification of ethane flux and attribution of methane emissions, Environ. Sci. Technol., 49, 8158–8166, 2015.

Sonnemann, G. R. and Grygalashvyly, M.: Global annual methane emission rate derived from its current atmospheric mixing ratio and estimated lifetime, Ann. Geophys., 32, 277–283, https://doi.org/10.5194/angeo-32-277-2014, 2014.

Sun, K., Tao, L., Miller, D. J., Khan, A. M., and Zondlo, M. A.: On-road ammonia emissions characterized by mobile, open-path measurements, Environ. Sci. Technol., 48, 3943–3950, 2014.

Tanaka, T., Yates, E., Iraci, L. T., Johnson, M. S., Gore, W., Tadi, J. M., Loewenstein, M., Kuze, A., Frankenberg, C., Butz, A., and Yoshida, Y.: Two-year comparison of airborne measurements of CO_2 and CH_4 with GOSAT at Railroad Valley, Nevada, IEEE T. Geosci. Remote Sens., 54, 4367–4375, 2016.

Thompson, D. R., Leifer, I., Bovensmann, H., Eastwood, M., Fladeland, M., Frankenberg, C., Gerilowski, K., Green, R. O., Kratwurst, S., Krings, T., Luna, B., and Thorpe, A. K.: Real-time remote detection and measurement for airborne imaging spectroscopy: a case study with methane, Atmos. Meas. Tech., 8, 4383–4397, https://doi.org/10.5194/amt-8-4383-2015, 2015.

VanCuren, R.: Transport aloft drives peak ozone in the Mojave Desert, Atmos. Environ., 109, 331–341, 2015.

Wennberg, P. O., Mui, W., Wunch, D., Kort, E. A., Blake, D. R., Atlas, E. L., Santoni, G. W., Wofsy, S. C., Diskin, G. S., Jeong, S., and Fischer, M. L.: On the sources of methane to the Los Angeles atmosphere, Environ. Sci. Technol., 46, 9282–9289, 2012.

White, W. H., Anderson, J. A., Blumenthal, D. L., Husar, R. B., Gillani, N. V., Husar, J. D., and Wilson, W. E.: Formation and transport of secondary air pollutants: Ozone and aerosols in the St. Louis urban plume, Science, 194, 187–189, 1976.

Wunch, D., Wennberg, P. O., Toon, G. C., Keppel-Aleks, G., and Yavin, Y. G.: Emissions of greenhouse gases from a

North American megacity, Geophys. Res. Lett., 36, L15810, https://doi.org/10.1029/2009gl039825, 2009.

Yacovitch, T. I., Herndon, S. C., Pétron, G., Kofler, J., Lyon, D., Zahniser, M. S., and Kolb, C. E.: Mobile laboratory observations of methane emissions in the Barnett Shale Region, Environ. Sci. Technol., 49, 7889–7895, 2015.

Yates, E. L., Iraci, L. T., Roby, M. C., Pierce, R. B., Johnson, M. S., Reddy, P. J., Tadic, J. M., Loewenstein, M., and Gore, W.: Airborne observations and modeling of springtime stratosphere-to-troposphere transport over California, Atmos. Chem. Phys., 13, 12481–12494, https://doi.org/10.5194/acp-13-12481-2013, 2013.

Zhong, S., Whiteman, C. D., and Bian, X.: Diurnal evolution of three-dimensional wind and temperature structure in California's Central Valley, J. Appl. Meteorol., 43, 1679–1699, 2004.